

## Effect of Solidification Path and Contraction on the Cracking Susceptibility of Carbon Peritectic Steels

Martin Herrera Trejo<sup>1,\*</sup>, Eddy Alfaro Lopez<sup>1</sup>, Jose Jorge Ruiz Mondragon<sup>1</sup>,  
Manuel de Jesus Castro Roman<sup>1</sup>, and Hugo Solis Tovar<sup>2</sup>

<sup>1</sup>CINVESTAV-IPN Unidad Saltillo, Saltillo-Mty freeway Km.  
13 Z.P 25900, Ramos Arizpe, Coahuila, Mexico.

<sup>2</sup>Ternium de Mexico S.A de C.V, Ave. de los Angeles Ote. No. 325. Col.  
Garza Cantu. Z.P. 66452. Col. San Nicolas de los Garza, Nuevo Leon, Mexico.

(received date: 21 November 2009 / accepted date: 20 April 2010)

The solidification path and contraction generated during the solidification of three carbon steels were studied. Two of the carbon steels were of hypo-peritectic chemical composition, with 0.11 % C and 0.15 % C, while one of the carbon steels were hyper-peritectic with 0.16 % C. The steels with 0.11 % C and 0.16 % C solidified as expected due to their chemical composition. In contrast, the chemically hypo-peritectic steel with 0.15 % C solidified as hyper-peritectic steel, which was associated with the microsegregation of Mn. For the steel exhibiting a hypo-peritectic solidification path, peritectic transformation occurred at solid fraction values higher than 0.9, where it was assumed that the contraction generated in the mushy shell cannot be fed by the liquid. However, for steels exhibiting a hyper-peritectic solidification path, peritectic transformation began at solid fraction values lower than 0.9, where the contraction generated by the peritectic transformation was partly fed by the liquid. Hence, the highest cracking susceptibility was associated with the hypo-peritectic solidification mode.

**Keywords:** solidification, segregation, mechanical properties, phase transformation, computer simulation

### 1. INTRODUCTION

For continuously cast carbon steel slabs, the solidification path is important in order to control the surface quality [1]. Steel slabs exhibiting a hypo-peritectic composition with a carbon content between 0.1 wt.% and 0.13 wt.% show the highest surface cracking susceptibility compared to steels with carbon contents higher than 0.16 % [2-14]. This cracking susceptibility is frequently associated with peritectic solidification, where the formation of  $\gamma_{(fcc)}$  phase occurs from both liquid (L) and  $\delta_{(bcc)}$  phases. It is expected that the surface cracks found in steel slabs are formed in the mushy zone, where contraction is generated. According to Clyne *et al.* [2], the mushy zone of continuously cast steels is divided into two zones depending on the ability of the remaining liquid to feed the solidification contraction: (1) a liquid feeding zone at solid fraction values lower than 0.9 and (2) a cracking zone at solid fraction values higher than 0.9. The cracks that form in the liquid feeding zone can be refilled with the surrounding liquid, whereas cracks formed in the cracking zone cannot be refilled with liquid because the

dendrite arms are compacted enough to resist feeding of the liquid. Later, Kim *et al.* [3] denominated the solid fraction value proposed by Clyne *et al.* [2] as “Liquid Impenetrable Temperature (LIT)”.

Moreover, for hypo-peritectic steels, the loss of mechanical properties in the mushy zone is also associated with microsegregation of solute elements at solidifying dendrite interfaces [15]. This solute microsegregation alters local equilibrium conditions, as well as the evolution of phases during solidification. According to previous studies [16,17], for carbon hypo-peritectic steels, Mn microsegregation can locally shift the peritectic “point” toward lower carbon content and lower temperatures, which eventually might change the solidification path to a hyper-peritectic path. Hence, although solute microsegregation during peritectic steel solidification has been extensively studied [1,4-20], there have only been a few studies that focused on the steel solidification path with slab surface cracking susceptibility [1,15-18]. Thus, this study combines a thermal analysis technique with solidification simulation to describe the effects of both the solidification path and the contraction generated during solidification on the surface cracking susceptibility of commercial carbon hypo-peritectic steels.

\*Corresponding author: martin.herrera@cinvestav.edu.mx

## 2. EXPERIMENTAL PROCEDURE

First, the thermal analysis technique was used in solidification experiments for three peritectic carbon steels with their chemical composition shown in Table 1. The studied steels, labeled as Steel A (0.11 % C), Steel B (0.15 % C), and Steel C (0.16 % C), are indicated with vertical lines in the equilibrium Fe-C pseudo-binary phase diagram shown in Fig. 1, obtained using the Thermo-Calc<sup>®</sup> software [21]. Both Steels A and B were chosen in order to elucidate the behavior of phases exhibited by hypo-peritectic steels, which are frequently associated with higher cracking susceptibility. In our study, Steel A showed a more marked hypo-peritectic nature compared to Steel B. On the other hand, the hyper-peritectic Steel C was selected as a reference of the hyper-peritectic solidification mode. In this context, these steels exhibited different C contents, whereas the contents of the other chemical elements were practically the same.

In the second stage, thermal and microstructural information (cooling curves, secondary dendrite arm spacing, and initial chemical composition) was fed into the DICTRA<sup>®</sup> software [22] in order to simulate the evolution of phases during the solidification of the three steels. Later, the accumulated contraction generated during solidification in the mushy shell was calculated as a function of both chemical composition and evolution of phases. Then, cracking susceptibility was inferred.

### 2.1. Thermal analysis

In order to obtain the cooling curves required for the simulation of solidification, solidification experiments were carried out. Figure 2 shows, schematically, the experimental setup used to obtain solidification cooling curves. Cylindrical Cu moulds of 3 cm in diameter and 7 cm in height were used to promote radial, rather than axial, heat flow. The Cu moulds were covered with a layer of ceramic insulation. Two different thicknesses of ceramic insulation were used to obtain two different cooling rates similar to those reported for zones near the surface of industrially cast conventional steel slabs [23]. Solidification experiments carried out in Cu moulds with the thinnest ceramic insulation led to approximate cooling rates between 11 °C/s and 12 °C/s, whereas those conducted with the widest thickness of ceramic insulation led to a cooling rate of approximately 7 °C/s. For these solidification tests, 12 kg of steel were melted in an induction furnace where pre-fusion slag was used as a protective cover for the liquid bath. Liquid steel was poured at

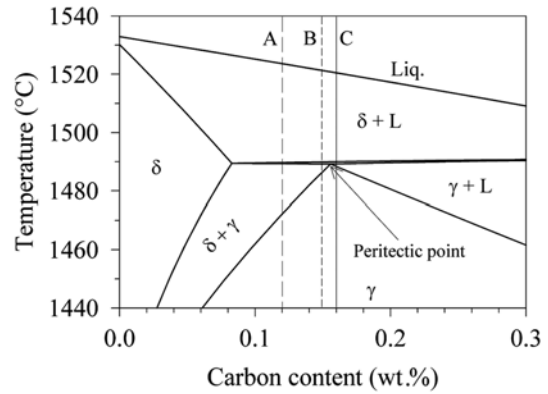


Fig. 1. Equilibrium Fe-C pseudo-binary phase diagram calculated using the Thermo-Calc<sup>®</sup> software.

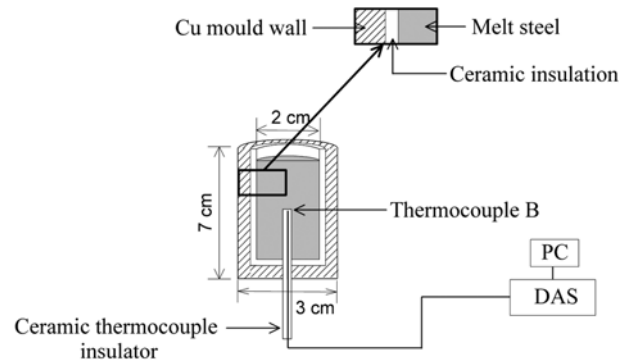


Fig. 2. Scheme of the experimental setup used to obtain the cooling curves.

1600 °C into the Cu moulds, which were fitted with a type B thermocouple for temperature recording during solidification of the samples. The thermocouple was positioned on the vertical axis at mid-height of each mould and linked to both a Data Acquisition System (DAS) and a Personal Computer (PC).

After obtaining cooling curves for the steels being examined, estimation of the required parameters for the solidification simulation was conducted. First, liquidus ( $T_l$ ) and solidus ( $T_s$ ) temperatures were determined from the cooling curves by using the procedure reported by Ruiz *et al.* [17], where cooling curves obtained at the lowest cooling rate, which was assumed to be close to the equilibrium condition, were initially considered.  $T_l$  and  $T_s$  were obtained from the equilibrium pseudo-binary phase diagram and then associated with peaks in the first and second derivatives of the cooling curves. Later, the solidification time,  $t_s$ , average cooling rate, and secondary dendrite arm spacing,  $\lambda$ , were

Table 1. Chemical composition of steels (wt.%)

Steel	Code	C	Mn	Si	S	P	Cr	Ni	Al	Cu
Hypo-peritectic	A	0.11	0.77	0.15	0.005	0.081	0.02	0.080	0.040	0.081
Hypo-peritectic	B	0.15	0.77	0.15	0.008	0.081	0.02	0.081	0.042	0.082
Hyper-peritectic	C	0.16	0.77	0.15	0.008	0.080	0.021	0.08	0.042	0.082

also estimated. After determining  $t_s$ , defined as the time elapsed between  $T_1$  and  $T_s$ , the average cooling rate was calculated by dividing the difference between  $T_1$  and  $T_s$  by  $t_s$  for each steel. On the other hand, the  $\lambda$  value, associated with each cooling condition, was calculated by using Eq. 1, which was reported for steels solidified at different cooling rates:

$$\lambda = 26.1 \times t_s^{0.38} \quad (1)$$

where  $\lambda$  is expressed in  $\mu\text{m}$  and  $t_s$  in seconds [8] and  $\lambda/2$  represents the length of control volume used for phase transformation simulation according to the model of Broody and Flemings *et al.* [24]. The described procedure was systematically applied to all cooling curves.

## 2.2. Simulation of solidification and thermal contraction calculation

Since the solidification simulation procedure for cooling curves has already been described in a recent paper published by Ruiz *et al.* [17], no details of this procedure will be provided in this paper.

The thermal contraction associated with phase growth during solidification was calculated using mathematical expressions given by Jablonka *et al.* [25]:

$$\varepsilon^{th} = \sqrt[3]{\frac{\rho(T_{ref})}{\rho(T)}} - 1 \quad (2)$$

where  $\varepsilon^{th}(T)$  is thermal contraction at temperature  $T$ ,  $\rho(T_{ref})$  and  $\rho(T)$  are the densities at a reference temperature  $T_{ref}$  and at temperature  $T$ , respectively. For this work,  $T_{ref}$  is the temperature in which the solid fraction has reached a value of 0.8, which, according to the measurements conducted by Mizukami *et al.* [1], corresponds to the temperature known as “Zero Strength Temperature” [2,3,5]. On the other hand, in the case of peritectic transformation in which several phases are involved, the average density at temperature  $T$  can be calculated with the following expression:

$$\rho(T) = \frac{1}{\sum_{n=1}^p \left[ \frac{f_n(T)}{\rho_n(T)} \right]} \quad (3)$$

where  $f_n(T)$  and  $\rho_n(T)$  are phase fraction and density, respectively, for each  $n$  phase coexisting at temperature  $T$ . The phase density can be obtained by using the equation suggested by Miettinen [18], which is a function of both temperature and chemical profiles exhibited during solidification. For the estimation of density, the evolution of C, Mn, and Si was considered during solidification. These values were obtained from the Dictra simulation carried out for each cooling rate and for each steel that was being studied.

## 3. RESULTS AND DISCUSSION

### 3.1. Thermal analysis

Figures 3(a), (b) and (c) show the cooling curves for the three steels solidified in Cu moulds and covered with ceramic insulation. On the other hand, with the purpose of illustrating the thermal analysis performed, Figs. 4(a) and (b) show the first and second derivatives, respectively, of the 12 °C/s cooling curve obtained for Steel A. In the same figures, both  $T_1$  and  $T_s$ , estimated from peaks exhibited in the first and second derivatives of the cooling curves, are indicated by discontinued vertical lines that limit the solidification time ( $t_s$ ). Thus,  $T_1$ ,  $T_s$  and  $t_s$  were obtained and, subsequently, the average cooling rate and  $\lambda$  were estimated. In this way, both the solidification temperatures  $T_1$  and  $T_s$ ,  $t_s$ , as well as the estimated parameters, cooling rate and  $\lambda$ , are given in Table 2 for each studied steel.

### 3.2. Evolution of phases

Figures 5(a), (b), and (c) show the phase evolution for each steel with respect to temperature during solidification

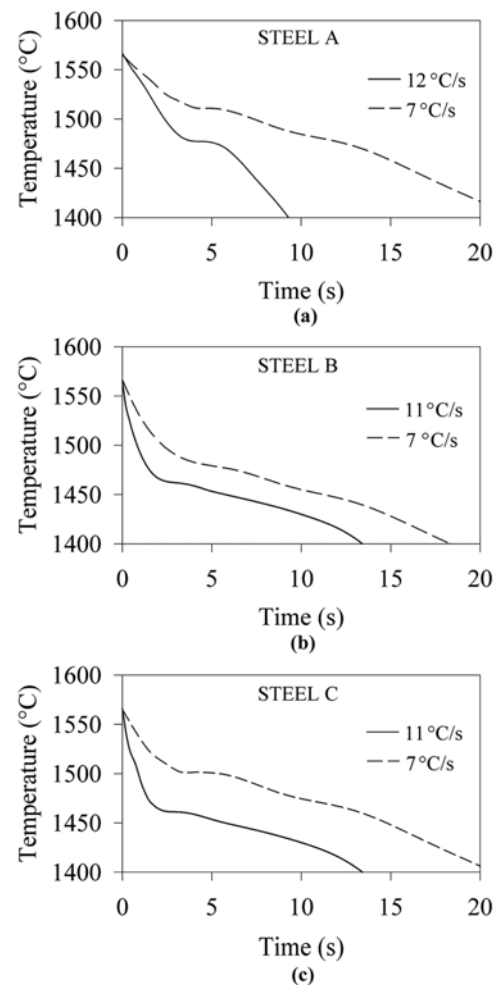


Fig. 3. Continuous cooling curves.

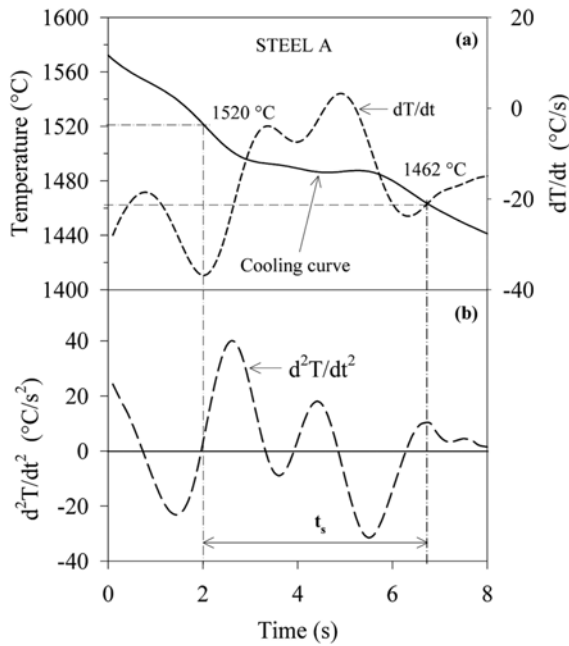
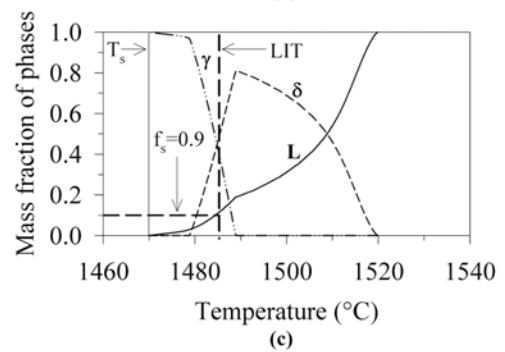
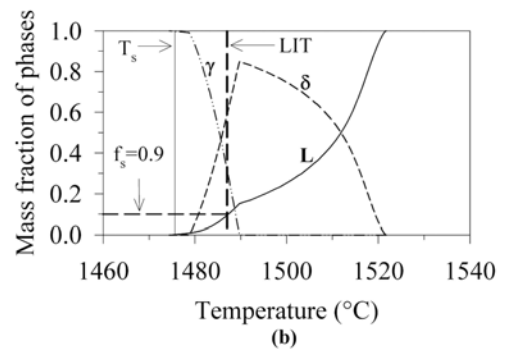
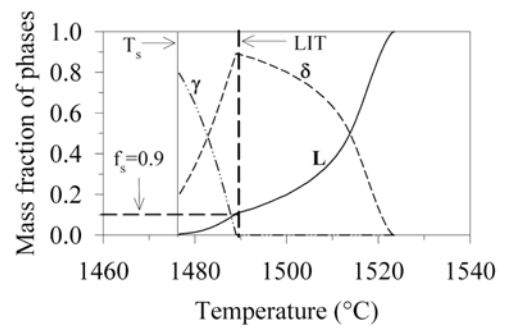


Fig. 4. Thermal analysis for steel A cooled at 12 °C/s.

for the highest cooling rates (11 °C/s to 12 °C/s). In these figures, a discontinued line indicates the LIT temperature, whereas the final solidification temperature is identified by a solid line. It can be seen for the three studied steels that the fraction of  $\delta$  phase grew progressively to around 1490 °C, after which the peritectic  $\gamma$  phase began to form. From this temperature onwards, the  $\gamma$  phase grew at the expense of both  $\delta$  phase and liquid. It was observed that Steel A, shown in Fig. 5(a), exhibited a hypo-peritectic solidification path in which the solidification ended with peritectic transformation, whereas both Steels B and C, shown in Figs. 5(b) and (c) respectively, exhibited a hyper-peritectic solidification path in which the solidification ended with the formation of  $\gamma$  phase from the remaining liquid after the peritectic transformation. It is noteworthy that the so-called hypo-peritectic Steel B exhibited a hyper-peritectic solidification path, shown in Fig. 5(b). This behavior has been observed in previous studies [16,17], where the change from a hypo- to hyper-peritectic solidification path was associated with the microsegregation of Mn in the remaining liquid at the end of solidification.



LIT = Liquid impenetrable temperature.  
 $T_s$  = Solidus temperature.

Fig. 5. Evolution of mass fraction of phases as a function of temperature in (a) steel A, (b) steel B and (c) steel C.

Figures 6(a), (b) and (c) show the evolution of Mn content in the liquid phase as a function of the solid fraction for the highest cooling rate in which the highest microsegregation levels were obtained. In these figures, the solid fraction associated with the start of peritectic transformation is indi-

Table 2. Values obtained from continuous cooling curves generated by thermal analysis

Code	Starting solidification temperature (°C)	Ending solidification temperature (°C)	Solidification time, $t_s$ (s)	Secondary dendrite arm spacing, $\lambda$ ( $\mu\text{m}$ )	Average cooling rate (°C/s)
A	1520	1462	5	48	12
	1524	1469	8	58	7
B	1523	1445	7	55	11
	1524	1455	10	63	7
C	1521	1445	7	55	11
	1523	1440	12	67	7

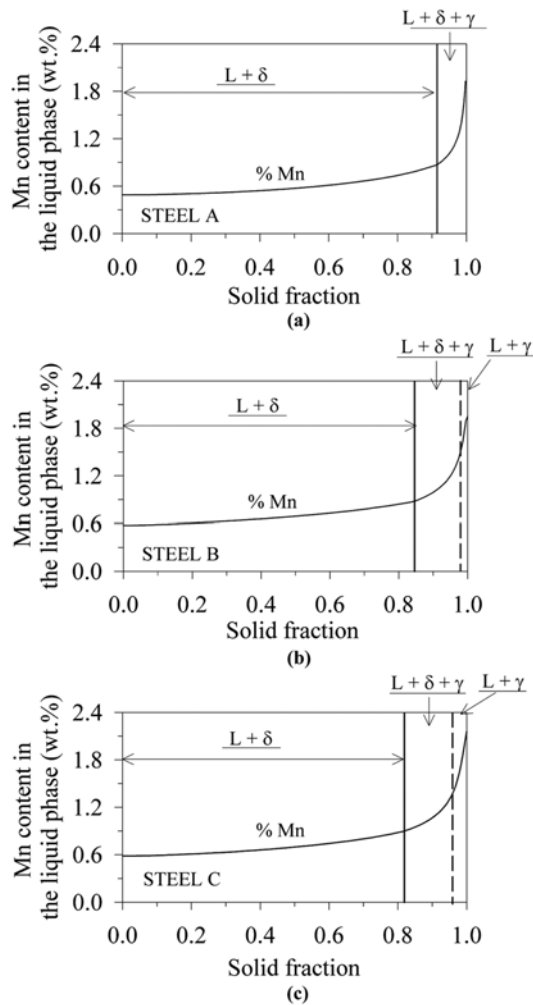


Fig. 6. Mn microsegregation in the liquid phase as a function of solid fraction evolution for each studied steel.

cated by a solid line, whereas the end of that transformation is identified by a discontinued line. It is observed that the Mn microsegregation level is similar for the three steels and becomes significantly important toward the end of solidification. On the other hand, according to a previous study [16], the Mn content in the steel shifts the peritectic point to lower carbon contents. Thus, it is thought that in Steel B, which exhibits a hypo-peritectic chemical composition near the peritectic point, as shown in Fig. 1, Mn microsegregation promoted the modification of the solidification path from hypo- to hyper-peritectic, which is shown in Fig. 6(b). Nevertheless, for Steel A, which has a more marked hypo-peritectic nature in comparison to Steel B, Mn microsegregation was not high enough to modify the solidification path. In this context, it is thought that a cause for the higher cracking susceptibility exhibited by hypo-peritectic steels with carbon contents ranging between 0.1 % C and 0.13 % C [1,4-8] is associated with insufficient Mn microsegregation in the liquid, which modified the hypo-peritectic solid-

ification mode.

Considering the cracking susceptibility criterion proposed by Clyne *et al.* [2], which states that the remaining liquid is unable to feed the strain generated in the mushy zone either at temperatures lower than the LIT or at solid fraction values higher than 0.9, two evolution phase behaviors can be distinguished in Figs. 5(a), (b) and (c). For Steel A, which exhibits a hypo-peritectic solidification path, shown in Fig. 5(a), peritectic transformation occurred at temperatures lower than the LIT, i.e. at temperatures where the remaining liquid cannot feed the strain generated in the mushy shell. This means that the strain produced in the mushy shell by peritectic transformation can accumulate, increasing its high cracking susceptibility. In contrast, for both Steels B and C, shown in Figs. 5(b) and (c) respectively, which exhibit a hyper-peritectic solidification path, about 50 % of the peritectic transformation occurs at temperatures higher than the LIT, i.e. at temperatures where the remaining liquid is able to feed the contraction generated by peritectic transformation. This means that the liquid phase can partly feed the contraction generated by peritectic transformation, which decreases the susceptibility to cracking.

### 3.3. Contraction

In order to illustrate the evolution of the contraction generated during the solidification of the steels being studied, Figs. 7(a), (b) and (c) show the contraction values calculated using Eqs. 2 and 3 as a function of chemical composition and solid fraction for the highest cooling rate. In the same figures, the solid fraction at which peritectic transformation starts,  $f_s^{\delta/\gamma}$ , is indicated by a vertical dotted line, whereas the solid fraction in which liquid is unable to feed the strain in the mushy zone,  ${}^{\text{LIT}}f_s$ , is identified by a solid line. In general, it can be seen that the contraction generated during solidification was controlled by the solidification path. Steel A, shown in Fig. 7(a), exhibiting a hypo-peritectic solidification path, showed a progressive contraction up to the end of solidification. On the other hand, both Steels B and C, shown in Figs. 7(b) and (c) respectively, exhibiting hyper-peritectic solidification path, showed a progressive contraction during the peritectic transformation followed by a slight expansion at solid fraction values of 0.99 and 0.97, respectively. This expansion exhibited by steels solidified by a hyper-peritectic solidification path was associated with an abrupt density change of the mushy shell, which was associated with Mn microsegregation in the remaining liquid, shown in Figs. 6(b) and (c), where the solid fraction values at which a slight expansion occurred agree qualitatively with the solid fraction values at which the Mn microsegregation is the highest.

Figures 7(a), (b) and (c) show shaded areas representing the accumulated contraction at the mushy zone within the solid fraction range from  ${}^{\text{LIT}}f_s$  to 1.0. Accumulated contrac-

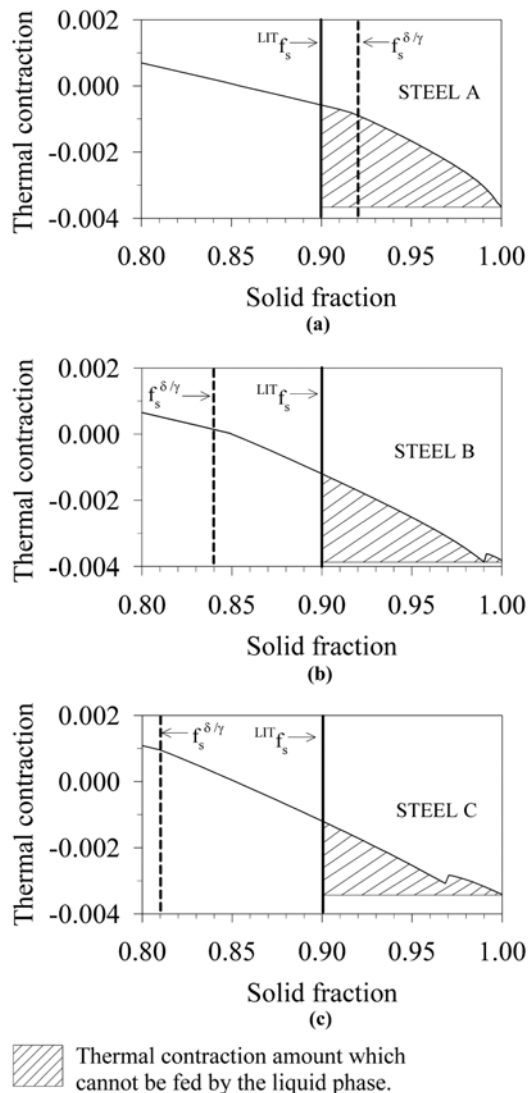


Fig. 7. Evolution of thermal contraction with respect to solid fraction evolution for each studied steel.

tion values of 0.0031, 0.0027, and 0.0022 were associated with Steels A, B and C respectively. It can be observed that the hypo-peritectic steel A, shown in Fig. 7(a), had the highest contraction level compared to both Steels B and C, shown in Figs. 7(b) and (c) respectively. In this context, it is believed that the highest cracking susceptibility associated with steels exhibiting a hypo-peritectic solidification path is the result of a combination of the contraction generated by the peritectic transformation and the liquid's inability to feed such contraction.

#### 4. CONCLUSIONS

Based on the description of the solidification mode and the estimation of contraction generated during the solidification of two hypo-peritectic steels with a carbon content of

0.11 and 0.15, respectively, and a hyper-peritectic steel with a carbon content of 0.16 %, the following conclusions were drawn:

1. The highest cracking susceptibility was attributed to the hypo-peritectic solidification path. For the steel with 0.11 % C exhibiting a hypo-peritectic solidification path, cracking susceptibility was associated with the remaining liquid's inability to feed the contraction generated by the peritectic transformation, which occurred at high solid fraction values.

2. Hypo-peritectic steels with a chemical composition close to the peritectic point can modify their solidification path to the hyper-peritectic one. In this work, the chemically hypo-peritectic steel with 0.15 % C exhibited a hyper-peritectic path, solidifying in a similar way to the hyper-peritectic steel with 0.16 % C. This was associated with Mn micro-segregation.

3. For hyper-peritectic steels, the cracking susceptibility is lower than that exhibited by hypo-peritectic steels. In this work, steels with 0.15 % C and 0.16 % C exhibited a hyper-peritectic solidification path, with about 50 % of the peritectic transformation occurring at solid fraction values, where it is assumed that the remaining liquid is able to feed the strain in the mushy shell. In this context, both steels containing 0.15 % C and 0.16 % C exhibited a lower cracking susceptibility than the steel with 0.11 % C.

#### REFERENCES

1. H. Mizukami, A. Yamanaka, and T. Watanabe, *ISIJ Int.* **42**, 964 (2002).
2. T. W. Clyne, M. Wolf, and W. Kurz, *Metall. Mater. Trans.* **13B**, 259 (1982).
3. K. H. Kim, T. J. Yeo, K. H. Oh, and D. N. Lee, *ISIJ Int.* **36**, 284 (1996).
4. E. T. Turkdogan, *Fundamentals of Steelmaking*, p. 104, The Institute of Materials, London (1996).
5. Y. M. Won, T. J. Yeo, D. J. Seol, and K. H. Oh, *Metall. Mater. Trans. B* **31B**, 779 (2000).
6. J. Konishi, M. Militzer, J. K. Brimacombe, and I. V. Samarasekera, *Metall. Mater. Trans. B* **33B**, 413 (2002).
7. D. M. Stefanescu, *ISIJ Int.* **46**, 786 (2006).
8. C. Cicutti and R. Boerl, *Steel Res. Int.* **77**, 194 (2006).
9. Y. M. Won, H. N. Han, T. J. Yeo, and K. H. Oh, *ISIJ Int.* **40**, 129 (2000).
10. Y. M. Won and B. G. Thomas, *Metall. Mater. Trans. A* **32A**, 1755 (2001).
11. W. R. I. A. Perkins, Proc. Int. Conf. organized by The Metals Society, London and L'institut the recherches de la sidérurgie française (IRSID), and held in Biarritz, France (1976).
12. J. K. Brimacombe, E. B. Hawbolt and F. Weinberg, *Continuous Casting Heat Flow, Solidification and Crack Forma-*

- tion (ed., Bookcrafters), p. 215, AIME, USA (1984).
13. H. Shibata, Y. Arai, M. Suzuki, and T. Emi, *Metall. Mater. Trans.* **31B**, 981 (2000).
  14. L. G. Zhu and R. V. Kumar, *Ironmak. Steelmak.* **34**, 71 (2007).
  15. K. H. Kim, K. H. Oh, and D. N. Lee, *Script. mater.* **34**, 301 (1996).
  16. E. Alfaro, M. Herrera, J. J. Ruiz, M. Castro, and H. Solis, *ISIJ Int.* **49**, 851 (2009).
  17. J. Ruiz, M. Herrera, M. Castro, and H. Solis, *ISIJ Int.* **48**, 459 (2008).
  18. J. Miettinen, *Scand. J. Metall.* **22**, 317 (1993).
  19. Y. M. Won, K. H. Kim, T. J. Yeo, and K. H. Oh, *ISIJ Int.* **38**, 1093 (1998).
  20. D. J. Seol, Y. M. Won, K. H. Oh, Y. C. Shin, and C. H. Yim, *ISIJ Int.* **40**, 356 (2000).
  21. A. Thermo-Calc Software AB. *The Phase Diagram in Multi-component Alloys*, R, Foundation of Computational Thermodynamics, Stockholm, Sweden (2006).
  22. DICTRA Software, *A Tool for Simulation of Diffusional Transformations in Alloys*, 24, Foundation of Computational Thermodynamics, Stockholm, Sweden, (2006).
  23. S. Louhenkilpi, J. Miettinen, and L. Holappa, *ISIJ Int.* **46**, 914 (2006).
  24. D. Brody and C. Flemings, *Trans. Metall. Soc. AIME* **236**, 615 (1966).
  25. A. Jablonka, K. Harste, and K. Schwerdtfeger, *Steel Res. Int.* **62**, 24 (1991).